ADVANCING EARTH AND SPACE SCIENCES

JGR Earth Surface

RESEARCH ARTICLE
10.1029/2023JF007424

The Influence of Coral Reef Spur and Groove Morphology on Wave Energy Dissipation in Contrasting Reef Environments

Lachlan Perris[1], Tristan Salles[1], Thomas E. Fellowes[1], Stephanie Duce[2], Jody Webster[1], and Ana Vila-Concejo[1]

[1]Geocoastal Research Group, Marine Studies Institute, School of Geosciences, The University of Sydney, Camperdown, NSW, Australia, [2]College of Science and Engineering, James Cook University, Bebegu Yumba Campus, Townsville, QLD, Australia

Key Points:

- Accurate bathymetry (<1 m) in forereef wave energy dissipation models can include features such as spurs and grooves (SaG)
- SaG increases forereef wave energy dissipation when compared to similar bathymetry without SaG
- Forereef dissipation shifts from bed friction to wave breaking in modeled environmental conditions based on future climate projections

Supporting Information:

Supporting Information may be found in the online version of this article.

Correspondence to:

L. Perris,
lachlan.perris@sydney.edu.au

Citation:

Perris, L., Salles, T., Fellowes, T. E., Duce, S., Webster, J., & Vila-Concejo, A. (2024). The influence of coral reef spur and groove morphology on wave energy dissipation in contrasting reef environments. *Journal of Geophysical Research: Earth Surface*, *129*, e2023JF007424. https://doi.org/10.1029/2023JF007424

Received 12 SEP 2023
Accepted 26 JUN 2024

Abstract Coral reefs protect coastlines from inundation and flooding and serve over 200 million people globally. Wave transformation has previously been studied on coral reef flats with limited focus on forereef zones where wave transformation is greatest during high-energy conditions. This study investigates the role of forereef spur and groove (SaG) morphology in wave energy dissipation and transmission at the reef crest. Using XBeach on LiDAR-derived bathymetry from One Tree Island in the southern Great Barrier Reef, we reproduced dissipation rates comparable to SaG field studies. We examined how wave energy dissipation differs between realistic bathymetry and those with SaG features removed, demonstrating an up to 40% decrease in dissipation when SaG features are absent. We then investigated changes to wave energy dissipation and wave transmission at the reef crest based on IPCC AR5 emission scenarios (RCP2.6 and RCP8.5) and a total disaster scenario (TD) for the year 2100. For RCP2.6, an increase in wave heights of 0.8 m and an increase in water level of 0.3 m resulted in a two-fold increase in dissipation rates. For RCP8.5 and TD, with no increase in incident wave height, dissipation rates were 29% and 395% lower than RCP2.6. This resulted in increased wave transmission at the reef crest by 1.8 and 2.7 m for the RCP8.5- and TD based models, respectively, when compared to the RCP2.6-based model. The results from our novel modeling approach of using long-shore varying accurate bathymetry on forereefs show increased wave energy dissipation rates with implications for reducing coastal flooding and island inundation on reef-lined coasts.

Plain Language Summary Coral reefs protect coastlines from floods and waves, benefiting over 200 million people globally. We studied how waves change over coral reefs, focusing on the forereef zone where wave transformation is most significant during high-energy conditions. The shape of the forereef, specifically the long comb-like grooves that cut through coral reefs, known as spur and grooves (SaG), modify wave energy transformation. Utilizing digital representation of waves over accurate reef shapes (known at bathymetry), we simulated wave dissipation rates comparable to real-world SaG studies. By comparing high resolution, accurate bathymetry to smoothed bathymetry with SaG removed, we demonstrate a 40% decrease in wave energy dissipation. Next, we investigated how wave energy dissipation changes in different forereef environments. We considered low and high emission scenarios (RCP2.6 and RCP8.5) from the IPCC AR5 report and a total disaster scenario (TD) for the year 2100, considering changes to wave power, and water-level. We found that models based on high-emission scenarios (RCP 8.5) had decreased dissipation rates, resulting in more water passing the reef crest. Our study highlights the benefits of using accurate reef shapes in simulating wave energy dissipation on coral reefs. Accurate bathymetry can incorporate features such as SaG of different shapes, which increase wave dissipation.

1. Introduction

Coral reefs provide many ecosystem services including coastal hazard protection from ocean waves, with over 200 million people worldwide depending on the stability of this service (Ferrario et al., 2014). Coral reefs are topographically complex structures which contribute to the frictional dissipation of waves, however this has been studied in greater details on the reef crest and reef flat (Ferrario et al., 2014; Monismith et al., 2015; Péquignet et al., 2014; Yao et al., 2020) than on the high-energy environments of the forereef slope (Acevedo-Ramirez et al., 2021; Duce et al., 2014, 2016, 2022; Monismith et al., 2013; Sheppard, 1981). Yet, wave breaking on the forereef slope is the dominant form of wave energy dissipation in high-energy conditions (Osorio-Cano

Table 1
Morphological Categorization of Spurs and Grooves (Duce et al., 2016)

Deep and disconnected (DaD)	Grooves are disconnected from the reef crest and appear in deeper water (>5.5 m).
Exposed to wave energy (EWE)	Grooves are oriented toward dominant wave direction
Long and protected (LaP)	Grooves are longer (>50 m) and not orientated toward dominant wave direction
Short and protected (SaP)	Groove lengths <50 m and not orientated toward dominant wave direction

et al., 2018) suggesting that it is a critical region for coastal protection by limiting wave transmission at the reef crest (Quataert et al., 2015). High dissipation rates on the forereef are controlled by forereef morphology such as spurs and grooves (SaG) (Monismith et al., 2013; Osorio-Cano et al., 2018).

SaG are shore-normal elongate ridges (spur) and troughs (groove) on the forereef slopes of many coral reefs (Duce et al., 2016). Their size, spacing and orientation are typically aligned with incident waves and consequently the morphometric classification of SaG (Duce et al., 2016) reflects the influence of waves in their formation (Table 1). High energy forereefs feature a more defined SaG than low-energy ones (Duce et al., 2016; Rogers et al., 2013). Recent research shows that high-relief (up to 10 m) spurs in the Mexican Caribbean have a large influence on wave transformation, with dissipation in the SaG zone contributing 35% of the wave energy flux. Wave energy flux on the forereef occurs mostly in the sea-swell frequency band (>0.04 Hz), which is the focus of the research presented here. While infragravity waves (0.004–0.04 Hz) are important for wave transformation over reef flats and in lagoons (Cheriton et al., 2016), field measurements of waves over SaG have shown negligible energy in the infragravity bands (Duce et al., 2022). Further field investigations are required but have been limited by the difficulty of accessing highly exposed and turbulent forereef slopes (Sheppard, 1981; Sous et al., 2022).

SaG morphologies are overlooked in 1D models of forereefs. SaG are also overlooked in both physical (e.g., Buckley et al., 2016) and numerical 2Dmodels (e.g., Baldock et al., 2020; Monismith et al., 2013; Osorio-Cano et al., 2018) that do not include sufficient spatial resolution to include features at the spatial scale of SaG. Furthermore, numerical models that include SaG morphologies typically use idealized bathymetry (e.g., da Silva et al., 2020; Rogers et al., 2013) with simplified morphologies that overlook the irregularity and diversity of SaG. Consequently, the impact of SaG morphologies (Table 1) on wave attenuation is poorly understood (Duce et al., 2022; Monismith et al., 2013; da Silva et al., 2020).

Studies have shown that forereef morphologies including SaG will be impacted by climate change (Castillo et al., 2012; De'Ath et al., 2012; K. Hughes et al., 2018; T. P. Hughes et al., 2018), likely resulting in reduced coastal protection (Baldock et al., 2014; Ferrario et al., 2014; Quataert et al., 2015; Sheppard et al., 2005) and increased wave overtopping (Amores et al., 2022; Beetham & Kench, 2018). Most notably, a loss of structural complexity (roughness) in forereefs will reduce bed friction impacting wave attenuation (Baldock et al., 2014; Harris, Power, et al., 2018; Harris, Revere, et al., 2018; Monismith et al., 2015; Rogers et al., 2016). These impacts are exacerbated by relative sea-level rise (SLR), changes in regional wave power (Meucci et al., 2020; Reguero et al., 2019) and modification and intensification of storm climates (Knutson et al., 2015), which all modify wave transformation processes on forereefs.

The overall aim of this paper is to provide an understanding of wave attenuation by SaG in contrasting coral reef environments. To achieve this, we first identify the benefits of high-resolution LiDAR-derived bathymetry in numerical wave models. Then, we employ these models to determine how SaG of different morphological classes affects the dissipation of wave energy. Finally, we investigate the effects of climate change on wave energy dissipation over SaG.

10.1029/2023JF007424

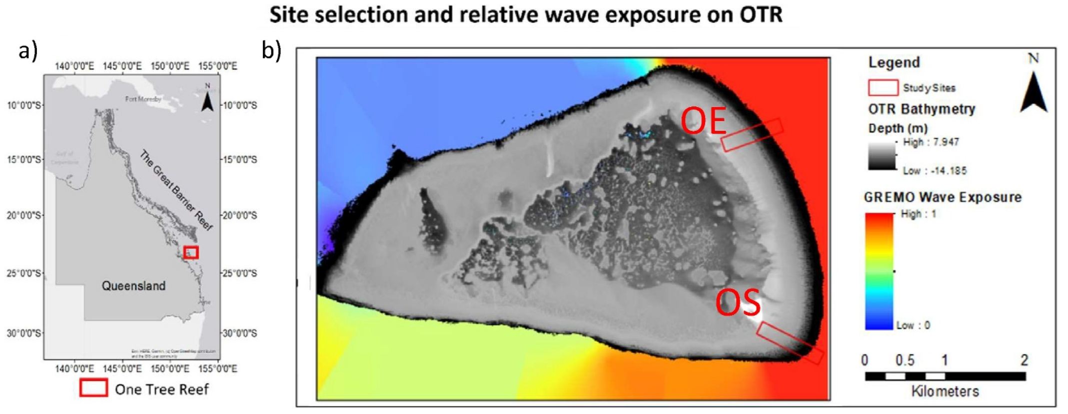

Figure 1. (a) One Tree Reef (OTR) in the Southern Great Barrier Reef, and (b) Study site locations for OTR East (OE) and OTR South (OS) and relative wave exposure (Pepper & Puotinen, 2009).

2. Methods

2.1. Study Site

One Tree Reef (OTR) (23°30′S, 152°06′E) is located 84 km offshore of the NE Australian mainland in the Capricorn Bunker Group, in the southern Great Barrier Reef (GBR) (Figure 1a). OTR is a lagoonal platform reef with semi-diurnal tides with a mean spring tidal range of 3 m. The entire forereef of OTR features SaG (Duce et al., 2016). The mean significant offshore wave height, Hs,mean of 1.7 m (Smith et al., 2023) is typically generated from persistent SE trade winds that dominate the Coral Sea for over 70% of the year (Jell & Webb, 2012). Consequently, the south-eastern forereef is the most exposed to ocean swells (Figure 1b). We considered two study sites featuring SaGs of varying morphological class (Table 1) on the eastern and southern sides of OTR (henceforth labeled OE and OS, respectively) (Figure 1b, Table 1).

2.2. SaG Morphometric Analysis

We determined morphometric parameters for SAG in the two study sites, including length, depth, width, and others (Table 2), from analysis of LiDAR derived bathymetry and used them to classify the SAG following the categorical framework of Duce et al. (2016) (Table 1).

2.3. Wave Transformation Modeling (XBeach)

We used XBeach (Roelvink et al., 2009) in Surf Beat mode because of its computational efficiency in solving short-wave amplitude variations. XBeach was selected as it has been extensively validated on complex coral reef bathymetry (da Silva et al., 2020; Harris, Power, et al., 2018; Harris, Revere, et al., 2018; Lashley et al., 2018; Quataert et al., 2015, 2020). XBeach has the capacity to include cross-shore currents and bed morphological

Table 2
Morphometric Parameters of Spurs and Grooves Adapted From Duce et al. (2016)

Morphometric parameter	Method
Length (L)	Path distance along the groove (m)
Depth (h_G)	The vertical distance between the lowest point in the groove and the highest point on the neighboring spur is calculated at four depths below sea level (−2, −4, −6, and −8 m).
Width (W)	Groove width is measured as the horizontal distance between its walls at half the depth, along isobaths of −2, −4, −6, and −8 m.
Orientation (θ)	Azimuth of straight line between maximum onshore and offshore extents of groove
Sinuosity (S)	Ratio of straight-line distance (x) to path length (L) such that: $S = x/L$
Wavelength (γ_{sag})	The horizontal distance between the highest points of adjacent ridges, parallel to isobaths, measured at depths of −2, −4, −6, and −8 m below mean sea level.

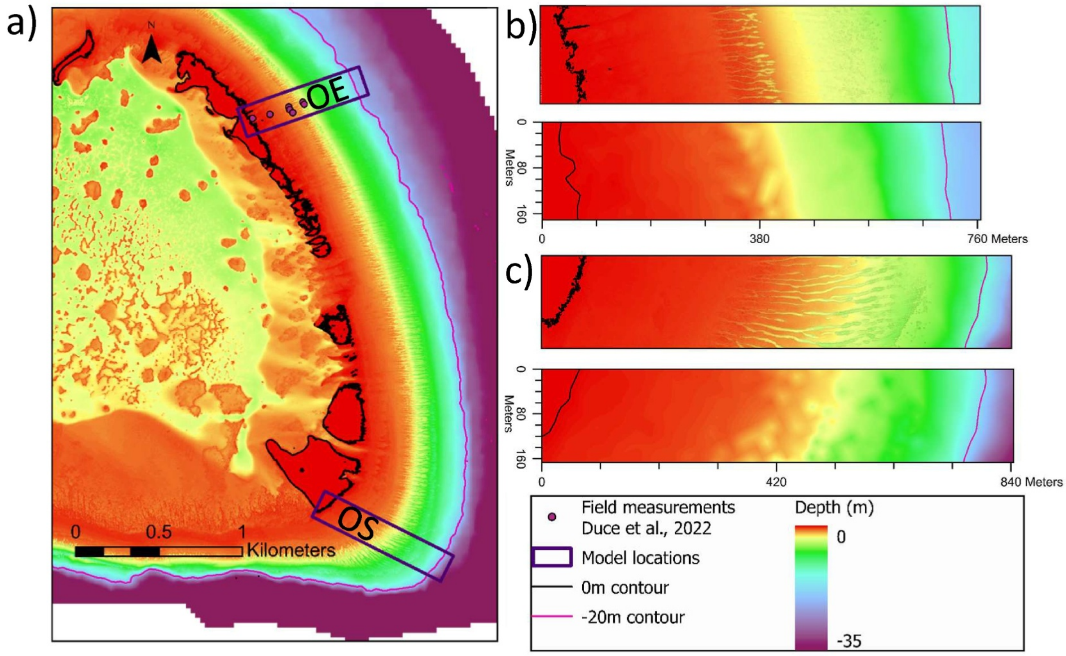

Figure 2. (a) The bathymetric grids extracted from LiDAR derived bathymetry of OTR (Harris et al., 2023) used in wave models from two study sites on the eastern (OE) and southern (OS) exposed forereefs of on One Tree Island. And (b) the forereef bathymetry extracted for site OE showing realistic and smoothed bathymetry and (c) for site OS.

changes, although those were not used in the present study. The lateral boundaries of all models were Neumann style boundaries which set the longshore gradients to zero, a recommended setting for Surf Beat modes to reduce the overestimation of longshore currents. For further details on the XBeach model parameters used, see Perris (2024).

2.3.1. Bathymetric Grids

We integrated data obtained from an Airborne LiDAR survey (Harris et al., 2023) with a spatial resolution of 0.5×0.5 m, to a depth of 14 m, and a bathymetry survey (Beaman, 2017) with a resolution of 30×30 m, covering depths up to a maximum of 20 m (Figure 2). The mosaic was constructed by transforming both datasets to the Geocentric Datum of Australia 1994, zone 56. This allowed prioritization of high-resolution datasets without averaging. The LiDAR-derived bathymetry was modeled in XBeach at the same spatial resolution of 0.5×0.5 m, representing an "accurate" bathymetry. The maximum depth at the offshore boundary, hmax, was selected to capture all depth-limited wave breaking within the model and was based on historical wave heights for the OTR considering:

$$h_{max} = H_{rms}/\gamma \tag{1}$$

where, γ is the breaker index and Hrms is the root mean square of the wave height. The breaker index was held constant across the reef at $\gamma = 0.55$, reflecting the conservative estimation ($\gamma = 0.55$) of (Duce et al., 2022) and within the ranges determined by Harris, Power, et al. (2018) and Harris, Revere, et al. (2018). We created smooth bathymetric grids without the SaG morphologies (Figure 2c) by resampling the grids using bilinear interpolation with cell size greater than γ_{sag} (Table 2). Smooth bathymetric grids were resampled to 0.5 m resolution to match the original grids.

The outer boundaries of the bathymetric grids were oriented to align mean groove headings with incident waves (Figures 2b and 2c), following field observations (Duce et al., 2014; Munk & Sargent, 1948; Shinn, 1963) and other wave transformation models constructed over SaG (Rogers et al., 2013; da Silva et al., 2020) (Figure 2b). Offshore boundaries were set beyond the maximum breaker depth for modeled wave heights (20 m: Equation 1)

Table 3
Model Input Parameters Are Presented for Three Study Sites, Two Wave Conditions and Four Forecasted Climate Outcomes for the Year 2100

Site	Climate scenario	Wave condition	$H_{offshore}$ (m)	Exposure factor	H Model (m)	T_{model} (s)	Friction factor	SLR (m)	Vertical accretion (m)	Reef erosion (m)	Total change in MSL (m)
OS	Present day	Mean	1.34	0.985	1.3	5.74	0.9	0	0	0	0
	RCP 2.6		2.14		2.1	7.26	0.54	0.43	0.16	0	0.3
	RCP 8.5		2.14				0.1	0.84	0.1	0.2	0.99
	TD		2.14				0.01	1.84	0	0.5	2.34
	Present day	Storm	4.8		4.7	10.87	0.9	0	0	0	0
	RCP 2.6		5.6		5.5	11.74	0.54	0.43	0.16	0	0.3
	RCP 8.5						0.1	0.84	0.1	0.2	0.99
	TD						0.01	1.84	0	0.5	2.34
OE	Present day	Mean	1.34	0.9042	1.2	5.5	0.9	0	0	0	0
	RCP 2.6		2.14		1.9	6.96	0.54	0.43	0.16	0	0.3
	RCP 8.5		2.14				0.1	0.85	0.1	0.2	0.99
	TD		2.14				0.01	1.84	0	0.5	2.34
	Present day	Storm	4.8		4.3	10.42	0.9	0	0	0	0
	RCP 2.6		5.6		5.1	11.25	0.54	0.43	0.16	0	0.3
	RCP 8.5		5.6				0.1	0.84	0.1	0.2	0.99
	TD		5.6				0.01	1.84	0	0.5	2.34

Note. A total of 16 unique models were run.

and the onshore boundaries at the present-day 0 m MSL contour (Figures 2b and 2c). Consequently, grids for each site are of different lengths and widths (Figure 2b).

We created smooth bathymetric grids without the SaG morphologies by resampling the grids using bilinear interpolation with cell size greater than γ_{sag} (Figure 2c). Smooth bathymetric grids were resampled to 1 m resolution to match the original grids. These smoothed grids were then run in XBeach under the four defined scenarios to quantify the influence of SaG presence on wave dissipation. The bed friction factor (f_w) was not changed between smoothed and realistic bathymetry models.

2.3.2. Contrasting Forereef Environmental Models

We considered four conceptual differences in forereef environments, based on forecasted scenarios for the year 2100. We include critical climate impacts to wave energy dissipation on coral reefs: sea-level change, reef health and wave energy conditions. The climate change scenarios are based on IPCC AR5 and include (a) the *present-day* scenario considering no change to current environmental factors, (b) the *low* (RCP 2.6), and (c) *high* (RCP8.5) emission scenarios from the AR5 IPCC report (Shukla et al., 2019), and (d) a *total disaster* (TD) scenario included to represent an extrapolation from IPCC scenarios to demonstrate model sensitivity and to simulate non-climate drivers of reef degradation (Shukla et al., 2019) (Table 3).

2.3.2.1. Changes to Sea Level

We used IPCC AR5 sea-level rise (SLR) rate of 3 mm/yr (Shukla et al., 2019). Under the *low* and *high* emission scenarios (RCP2.6 and RCP8.5), SLR is expected to reach up to 10–20 mm/yr. Subsequently, we have included SLR of 0.43 m (RCP2.6) and 0.84 m (RCP8.5) for the year 2100 (Shukla et al., 2019). Human stressors (e.g., infrastructure development and human-induced habitat degradation) are also likely to contribute to increases in local SLR (Shukla et al., 2019). An additional 1 m of eustatic SLR was included for our TD scenario to reflect significant changes in climate conditions and non-climatic anthropogenic stressors (Shukla et al., 2019) (Table 3). The total sea-level increase in each of the models (Table 3) was determined by the sum of eustatic and local sea-level changes, and the vertical accretion and erosion of the reefs.

10.1029/2023JF007424

2.3.2.2. Reef Morphological Changes

Reef morphological changes have been simplified into three key characteristics: reef vertical accretion, erosion, and structural complexity. A forecasted vertical accretion rate of 2 mm/yr was used based on field measurements from coral reef cores from across the GBR (Dechnik et al., 2015; Sanborn et al., 2020), Western Australia (Perry et al., 2018), Tahiti (Buddemeier & Smith, 1988), the Maldives (Kench et al., 2022), Indo-Pacific averages compiled by Montaggioni (2005) and the Solomon Islands (Saunders et al., 2016). Alternatively, erosion of forereefs can occur due to the physical removal of coral and framework by storms and high wave energy (Madin & Connolly, 2006). This is most evident on degraded coral reefs where erosion at the reef crest has been observed at 6 mm/yr (Eakin, 1996; Sheppard et al., 2005). We used a conservative estimate of 2.6 mm/yr (0.2 m by 2100) of reef erosion for RCP 8.5 and a maximum of 6.4 mm/yr (0.5 m by 2100) of erosion under a TD scenario, modeled as a uniform decrease in elevation over the simulated domain, representing a simplified model of reef morphological transformation as SaG may respond to future reef transformation differently; however, this has not been investigated. The resulting sea level was determined by combining the projected rates of SLR with erosion and accretion values for each scenario (Table 3).

To simulate a loss in forereef structural complexity, we altered the dimensionless wave friction factor (f_w) to replicate changes in coral structural complexity. To represent the healthy and rough forereef of OTR (Harris et al., 2023; Roelfsema et al., 2021), f_w were linearly interpolated between $f_w = 0.9$ (healthy reef) to $f_w = 0.1$ (degraded or smoothed reef). For the *TD* scenario, which represents a degraded reef and a shift to a carbonate sand substrate we used $f_w = 0.01$ (Smyth & Hay, 2002) (Table 3).

2.3.3. Wave Input Parameters

Mean offshore wave conditions were determined by satellite altimeter observations over 30 years (1985–2015) using RADWave (Smith et al., 2020) (Table 3). A small region (0.6° × 0.4°) representing dense altimeter data tracks was identified on the eastern, exposed side of the OTR (Figure S1). We determined site-specific model input wave heights (H_{model}) by combining offshore wave conditions with a relative wave exposure model, GREMO (GIS-based generic model for estimating relative wave exposure; see Figure 1b), following Pepper and Puotinen (2009),

$$H_{model} = K_r \; H_{offshore} \tag{2}$$

where, $H_{offshore}$ is the offshore wave height obtained from RADWave (Figure 1b and Figure S1) and K_r is the relative exposure coefficient, normalized between 1 (most exposed) and 0 (least exposed). Finally, altimeter wave heights derived for offshore swell (Hs,mean = 1.3 m, Table 3) were compared to measured waves at the eastern forereef at OTR (Hs,mean = 0.62 m at the outer forereef) (Duce et al., 2022).

2.3.4. Changes to Wave Climate

We increased offshore model wave heights ($H_{offshore}$) to simulate contrasting forereef environments based on future climate change scenarios (Table 3) with wave periods (T_{model}) determined for a fully developed sea-state from the Joint North Sea Wave Project spectrum (Young, 1992). Storm waves were calculated from the maximum wave height observed in the RADWave altimeter data. The final model wave heights were dependent on forereef location and relative exposure to wave energy determined by Equation 2.

2.3.5. XBeach Model Outputs

Each model was run for a total of 300 s to allow sufficient spin up time for wave propagation across the modeled domain. We analyzed the outputs of XBeach for water surface elevation (zs), total dissipation rate (D), and dissipation rate due to bed friction (D_f) to obtain wave energy dissipation rates and wave transmission over the reef crest. Total dissipation was used to compare XBeach results with field measurements and to determine dissipation by breaking (D_b) such that $D_b = D - D_f$. As models are two-dimensional (x, y spatial domains) and evolve through time (t), we calculated mean and peak total dissipation rates across t and x domains for the entire bathymetric grid. Mean total dissipation rates were also taken between two points where hydrodynamic data sampled by Duce et al. (2022). Wave transmission over the reef crest was calculated as the difference between the initial water level at the reef crest and the maximum water level at the reef crest during each model run.

AGU ADVANCING EARTH AND SPACE SCIENCES

Journal of Geophysical Research: Earth Surface

10.1029/2023JF007424

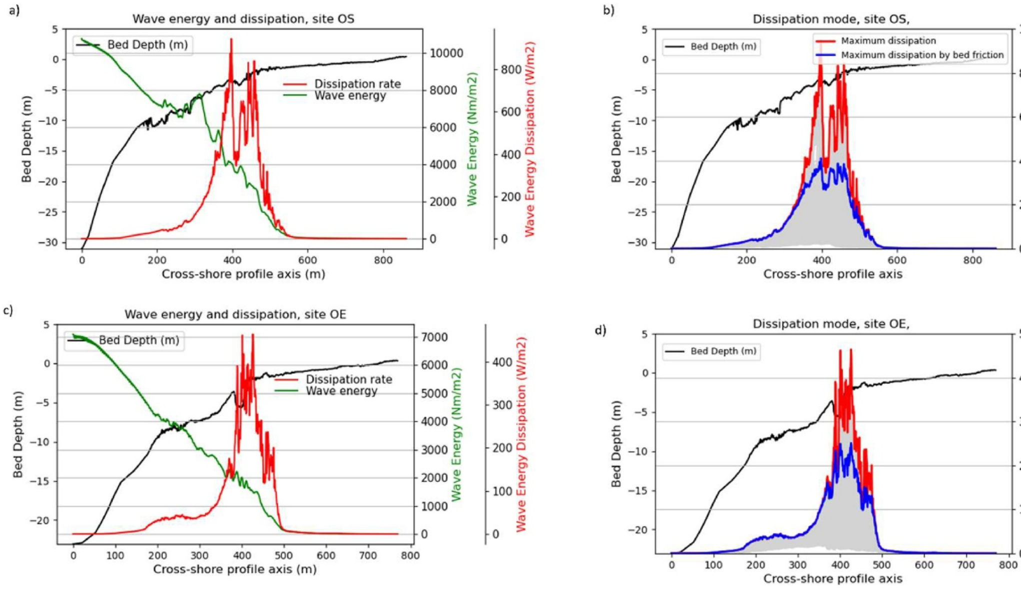

Figure 3. Spatially-averaged wave energy (depicted in green) and corresponding maximum wave energy dissipation across the x-domain. Exemplary bathymetry profiles (illustrated by black lines) originate from the center of the model (y/2) at Site OS (a) and site OE (c). Panels (b) and (d) represent the maximum dissipation and maximum dissipation attributed to bed friction (depicted in blue) for site OS and site OE, respectively. It is important to observe that distinct scale bars are applied for each respective sites.

3. Results

3.1. SaG Morphometric Analysis

SaG morphometrics were quantified for 123 grooves across the two study sites (Table 3). Grooves at the southern site (OS) were on average 3 times longer, 1.4 times deeper and 1.3 times wider than those at the eastern site (OE) (Table 3). Using the morphometric classification of Duce et al. (2016), the exposed to wave energy (EWE) grooves were the most common across three of the four sites (100 of 123 SaG) (Table 3). Deep and disconnected (DaD) grooves were present on the lower forereef platform of site OE.

3.2. Wave Transformation Over Accurate Bathymetry

The peak dissipation rates under present day conditions, taken as the maximum dissipation across all axes (x, y, t), were 463.9 and 946.3 W/m^2 at sites OE and OS, respectively (Figure 3). Wave energy dissipation due to bed friction was dominant in present day scenarios over dissipation due to wave breaking (Figures 4b and 4d). Between the two locations of field measurements conducted by Duce et al. (2022) (Figure 2c) the mean dissipation

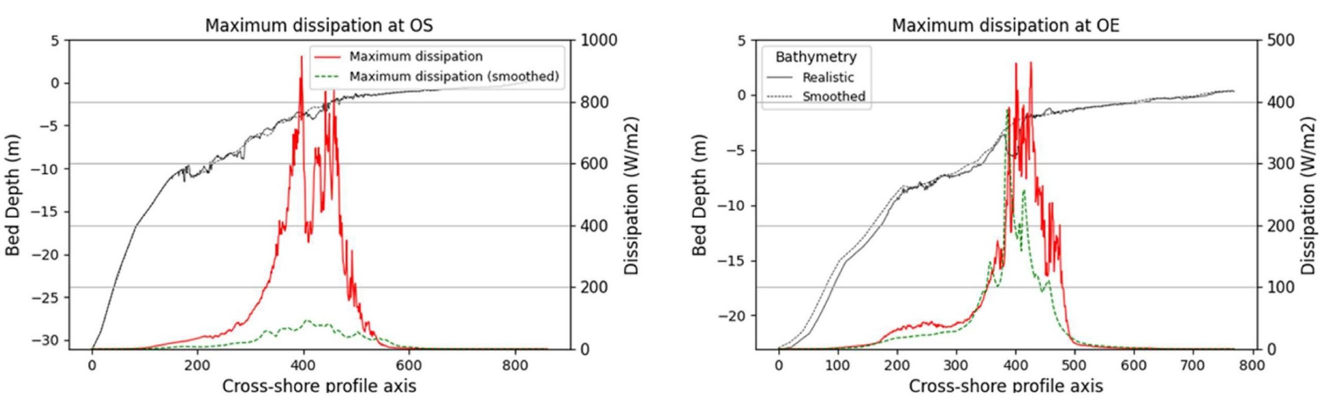

Figure 4. Maximum dissipation measured at site OS (a) and OE (b) for actual bathymetry and smoothed bathymetry.

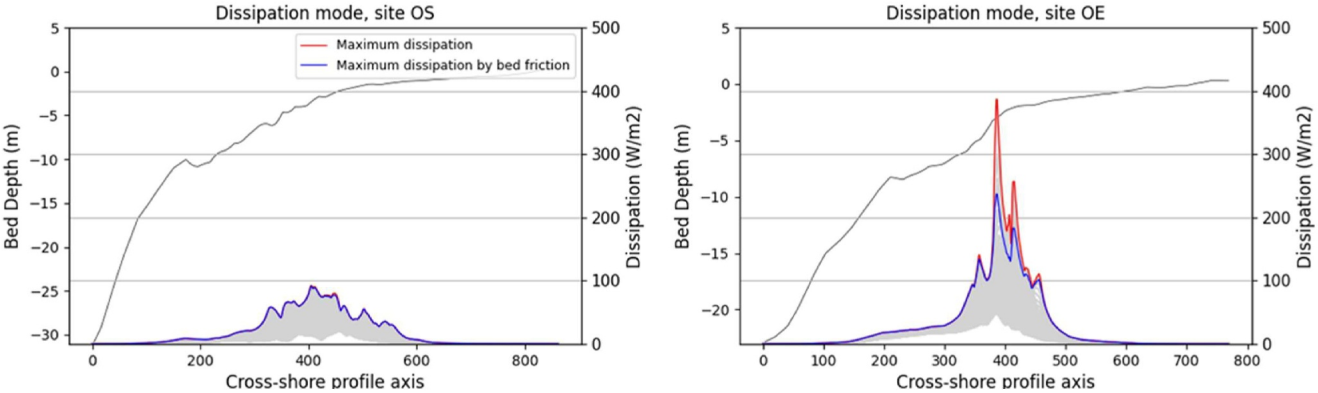

Figure 5. Maximum dissipation and maximum dissipation attributed to bed friction (depicted in blue) over smoothed bathymetry for site OS and OE. Exemplary bathymetry profiles (illustrated by black lines) originate from the central region of the model (y/2).

rate was 10.6 W/m^2, the maximum dissipation rate of 463.9 W/m^2 occurred during this zone. Wave energy dissipation by bed friction contributed 78% of energy at the site OE before waves reached the reef crest and 67% at the site OS in the upper forereef slope. The maximum wave energy dissipation due to wave breaking constituted 22%, and 32% of total dissipation at site OE and OS, respectively (Figures 4b and 4d).

3.3. Comparison of Realistic and Smoothed Bathymetries

Realistic bathymetry were compared with modified bathymetry with SaG removed. In all cases, removing SaG resulted in a decrease in both peak and mean wave energy dissipation across the entire simulated domain. With SaG removed, peak dissipation at site OS was 92.56 W/m^2 and mean dissipation was 2.61 W/m^2. This represents a 90.2% reduction in peak wave energy dissipation, and a 40.06% reduction in mean wave energy dissipation across the entire profile. At site OE, removing SaG features from the bathymetry resulted in peak wave energy dissipation of 463.85 W/m^2 and a mean dissipation rate of 2.2 W/m^2. This represents a 16.6% decrease in peak wave energy dissipation and a 12.67% decrease in mean wave energy dissipation.

The percentage of breaking versus frictional dissipation is also modified by the presence of SaG. Mean dissipation due to bed friction was 2.62 W/m^2 at site OS and 2.18 W/m^2 at site OE, representing 99.95% and 99.41% of total dissipation, respectively (Figure 5). This contrasts to real bathymetry models (Figures 3b and 3d) where dissipation by bed friction represented 78% and 67% at site OS and OE, respectively. The bed friction factor (f_w) was not changed between smoothed and realistic bathymetry models.

3.4. Wave Transformation Over Contrasting Forereef Environments

Wave transformation was found to vary greatly among models depending on SaG morphology, wave exposure, mean water levels and reef structural complexity. These parameters are likely to change with climate change (Amores et al., 2022; Castillo et al., 2012; Harris, Rovere, et al., 2018; K. Hughes et al., 2018; T. P. Hughes et al., 2018). Total wave energy dissipation and dissipation due to bed friction changed at both sites for all modeled forereef environments (Table 3).

Mean and peak total dissipation rates were computed for each site across all three climate scenarios (Table 3, Figure 4). When comparing dissipation rates from present day to RCP2.6 for the year 2100, mean total dissipation increased by 187% at site OS (4.4–12.5 W/m^2) and maximum total dissipation increased by 59.7% (946.3–1,511.4 W/m^2) (Figures 6a and 6b). At site OE, the mean total dissipation rate increased by 208.6% (2.5–7.8 W/m^2) and maximum total dissipation increased by 217.7% (463.9–1,473.4 W/m^2) (Figures 6d and 6e).

When comparing RCP2.6 to RCP8.5, we found a decrease in mean total dissipation across site OS of 18.1% (12.5–10.6 W/m^2) and an increase in the maximum total dissipation rate of 23.2% (1,511.4–1,966.9 W/m^2). Site OE retained a high mean total dissipation rate from RCP2.6 to RCP8.5, increasing a further 11.7% (7.78–8.81 W/m^2) and an increase of 19.3% to the peak dissipation rate (1,473.42–1,824.70 W/m^2).

10.1029/2023JF007424

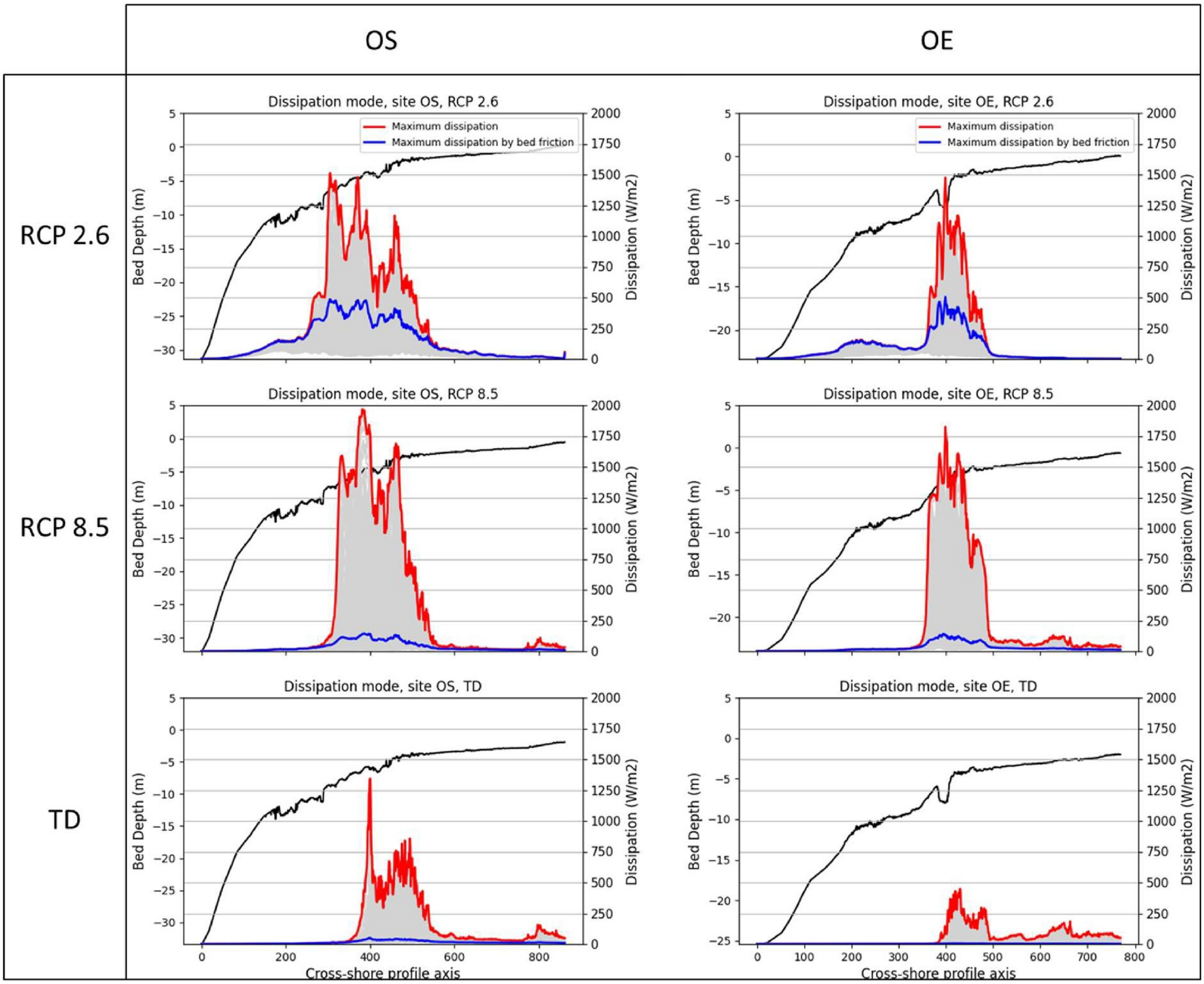

Figure 6. Maximum wave energy dissipation (blue),dissipation due to bed friction (red) and all dissipation profiles (gray) across the x and time domains for site OS under RCP 2.6, RCP 8.5 and total disaster (TD) forereef environments. For site OE under RCP 2.6, RCP 8.5 and TD forereef environments. Exemplary bathymetry profiles (illustrated by black lines) originate from the central region of the model (y/2). Note *Y* axis are unique for each study site to highlight relative differences in dissipation across contrasting forereef environments (Table 3).

When compared to RCP8.5 in the TD scenario, mean total dissipation rates decreased by 66.2% (10.61–3.58 W/m^2) at site OS and a decrease in peak total dissipation of 31.8% (1,966.89–1,340.93 W/m^2) (Figures 3b and 3c). At site OE, mean total dissipation decreased by 86.2% (8.81–1.21 W/m^2) and peak total dissipation rate decreased by 75.4% (1,824.7–448.24 W/m^2) (Figures 4e and 4f).

Under present-day conditions, bed friction is dominant, contributing 98% and 99% of total wave energy dissipation (Figures 5 and 6). Comparing RCP 2.6 to RCP 8.5, site OS decreased in total dissipation by 15.3% and at site OE total dissipation increased by 13.2% (Figure 7). This can be attributed to a decrease in frictional dissipation by 57% at site OS and 42% at site OE(Figures 6 and 7). In this case, dissipation by wave breaking increased by an average of 659% for both sites. This results in a shift in the dominant form of wave energy dissipation (Figure 7). Comparing RCP2.6 to the TD scenario, mean frictional dissipation (D_f) decreases by 82.5% at site OS and 95.8% at site OE, while wave breaking remains marginally greater by 0.1% (OS) and 1.5% (OE) in the TD scenario. Despite this, the mean total wave energy dissipation (the sum of frictional and wave breaking dissipation rates) decreases by 71.4% (OS) and 84.4% (OE).

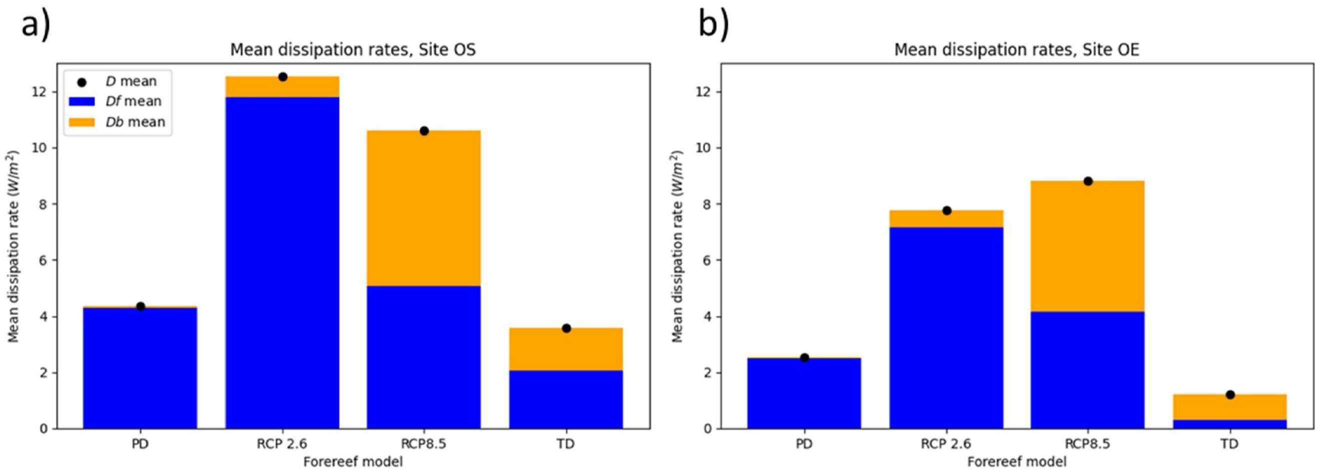

Figure 7. Mean total dissipation (D mean) for OS (a) and OE (b) study sites and mean dissipation by bed friction (Df mean) and wave breaking (Db mean) for each forereef model (see Table 3).

We calculated maximum water levels at the reef crest for both sites under four forereef model environments, based on present day conditions and three climate change scenarios considering both mean and storm wave conditions (Table 2). For mean wave conditions, maximum reef crest water levels in the present-day model were near zero (0 and 0.1 m at site OS and OE, respectively). The maximum reef crest water levels increase for all simulated reef scenarios (Figure 7). We calculated a maximum excursion from mean water levels at the reef crest of 0.4 m at site OS and 0.1 m at site OE for RCP 2.6 with larger increases to 0.4 m (OS) and 0.7 m (OE) for RCP8.5. The high emissions scenario (TD) had the highest reef crest water levels of 2.1 m (OS) and 2.0 m (OE).

Storm wave conditions increased reef crest water levels compared with mean wave heights in all cases (Figure 6; Table 2). Under present-day conditions, reef crest water levels were greater for mean wave conditions at 1.25 and 0.5 m for site OS and site OE, respectively. Under forecast climate change scenarios, storm waves did not significantly impact reef crest wave transmission under RCP2.6 compared with present day conditions despite an increase in wave height of 3.5 m. Reef crest water levels, under RCP8.5 were 2.1 m at site OS and 1.4 m at site OE, which increased significantly to 3.5 and 3.9 m in TD models at each site, respectively.

4. Discussion

4.1. Benefits of Accurate High-Resolution Bathymetries in Numerical Wave Models

Our models of wave transformation over LiDAR-derived bathymetry focus on the influence of SaG morphology on wave energy dissipation and wave transmission over the reef crest. Under mean wave conditions, we calculated average dissipation rates across the entire forereef profile of 3.61 W/m^2 at site OS and 2.52 W/m^2 at site OE for offshore wave heights of 1.3 and 1.2 m, respectively. This calculation is made across the entire reef profile representing 862 and 770 m, respectively (Figures 2b and 2c). Field measurements of wave energy dissipation conducted at OTR were taken at the same site as OE presented in this study (Figure 2c) (Duce et al., 2022). We determined a mean dissipation rate of 10.6 W/m^2 across 60 m between the two instruments, almost entirely due to bed friction (Figure 3d). Duce et al. (2022) recorded mean dissipation rates of 20 W/m^2 with wave heights of $H_s = 0.78$ m and $T_p = 5$ s. Differences in the recoded and modeled data at this site may be attributed to the incident wave direction (N-NE during the deployment period), which was not completely aligned with SaG as modeled here. These results compare with data obtained on a fringing reef in Ipan (Guam), which also featured SaG on the forereef (Péquignet et al., 2011). Between two sensors placed 55 m apart inside a 5 m deep groove, the dissipation rate was 25 W/m^2 for offshore wave heights of 1–2 m (Péquignet et al., 2011). Monismith et al. (2015) identified comparable dissipation rates of 25 W/m^2 on a forereef in Palmyra (Kiribati) between instruments 50 m apart for incident wave heights of 1 m. Monismith et al. (2013) determined rates of 22 W/m^2 across a forereef at Mo'orea (French Polynesia) with instruments located 50 m apart and wave heights of 0.3–0.5 m. Dissipation rates for each of these studies are assumed to be due to bed friction with constant dissipation between the instruments. Our

Table 4
Morphometric Parameters and Classes of Spurs and Grooves at the Two Study Sites

	Mean SaG morphometric parameters					Quantity of SaG classes by site			
Site	Length (m)	Sinuosity	Orientation (Deg)	Depth (m)	Width (m)	DaD	EWE	LaP	SaP
OS (south)	187.12	0.99	116.73	1.95	4.02	0	40	0	0
OE (east)	63.18	0.99	71.5	1.38	3.12	23	60	0	0

results produce dissipation rates comparable to field measurements in similar environments, demonstrating the successful application of realistic bathymetry to numerical modeling of forereef wave energy dissipation.

Using a real bathymetry, our study demonstrates the influence of groove sinuosity on wave energy dissipation by breaking. Our results show that shore-normal waves interact with spur walls that do not perfectly align with incoming swell. In our study, the mean groove heading was used to align the bathymetric grids to the oncoming waves (Figure 2b), consistent with field observations (Duce et al., 2020; Munk & Sargent, 1948). Despite this, variation in headings between grooves and the sinuosity of individual grooves produces steep irregularities in the forereef slope that have a large impact on the oncoming waves, playing a significant role in both dissipation by wave breaking and bed friction. The straight and shore normal SaG identified in this analysis (mean sinuosity of $S = 0.99$, where 1 is a perfectly straight groove) (Table 4) are representative of groove sinuosity across the southern GBR. For example, observations of 12,102 grooves in the GBR and South Pacific show a mean groove sinuosity of $S = 0.98$ (Duce, 2017). Despite remarkable regional consistency in groove morphology, we observed that even small deviations from perfect shore-normal grooves are significant for wave transformation on the forereef (e.g., Figure 7). These features would not be considered in 1D or idealized 2D bathymetry. The use of real bathymetry in modeling efforts can elucidate the heterogeneity of dissipation rates on forereefs.

4.2. Effects of SaG on Wave Energy Dissipation

SaG morphology was found to increase wave energy dissipation. We compared forereefs featuring SaG to forereefs with SaG removed, while controlling for water level, wave height and bed friction (Figure 4). At both sites, the presence of SaG increased dissipation on the outer forereef (Figure 4). The frictional mode of dissipation was dominant in both smoothed (SaG removed) and realistic bathymetry. Dissipation by wave breaking was reduced in the smoothed models, despite similar model resolution and forereef geometry (Figure 5). At site OE, dissipation by breaking occurs in a similar location along the forereef (Figures 3b, 3d, and 5), near the reef crest. However, the magnitude of wave breaking is reduced, as the mean bathymetric gradient at the reef crest is reduced by the removal of SaG features. This lends further support to the idea that SaG morphology can introduce steep bathymetric inclines to forereefs that can increase wave energy dissipation by breaking. Differences in SaG morphology similarly have an impact on wave transformation and dissipation. The most wave exposed site (southern site, OS) has the highest average dissipation rate of 71.5% over 300 m SaG zone due to bed friction (Figure 3a). The long (mean length of 187.12 m) and deep (mean depth of 1.95 m) EWE grooves at this exposed site may explain how this high average dissipation rate occurred (Table 1). The length of EWE SaG creates surfaces of high frictional drag that extend the zone of frictional dissipation and contribute to high average dissipation rates (Figures 4a and 5). Shore normal currents occurring in the long and deep grooves have also been observed and facilitate high rates of dissipation (Rogers et al., 2013). We demonstrate under present-day conditions that bed frictional dissipation is dominant in dissipating wave energy before breaking occurs at the reef crest (Figures 3a and 3c). Bed frictional dissipation represents 98.0% and 98.9% of total dissipation at site OS and OE, respectively (Figures 3a and 3c). This is consistent with field research conducted at the OTR (Duce et al., 2022) and in other high-energy settings (Lowe et al., 2005; Monismith et al., 2015; Rogers et al., 2017). For example, under mean wave conditions at Palmyra (Kiribati), a high bed friction coefficient ($f_w = 1.8$) facilitated greater wave energy dissipation due to bed friction than from wave breaking (Monismith et al., 2015), which is consistent with field observations in Kaneohe Bay, Oahu, Hawaii (Lowe et al., 2005). Our results suggest that the modes of wave energy dissipation (frictional or breaking) are not only influenced by the wave conditions but also by the heterogenous morphology of the forereef slopes (Figures 6 and 8).

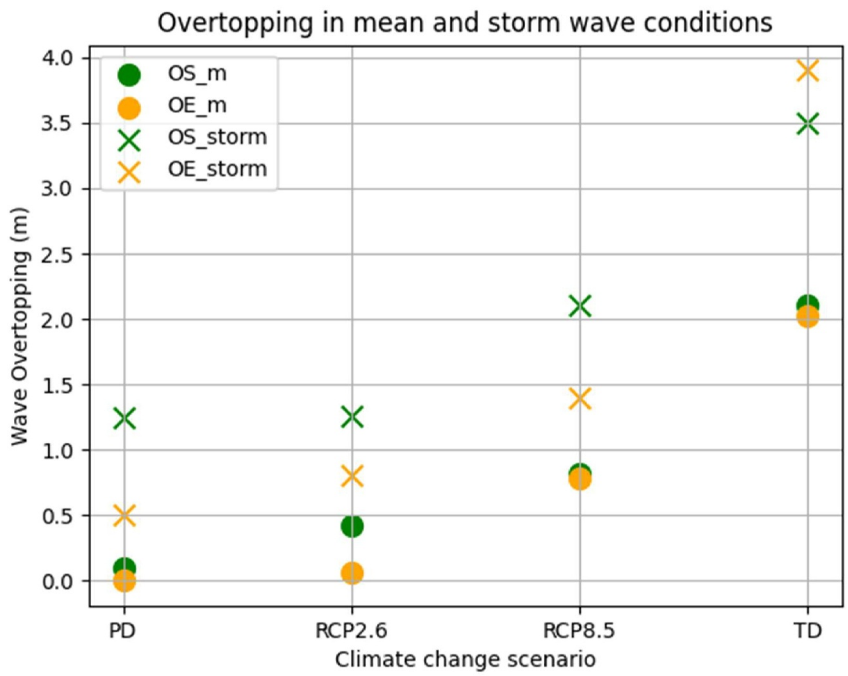

Figure 8. Maximum excusion from mean water levels at the reef crest (0 m contour) at both sites under mean (OS_m and OE_m) and storm (OS_storm and OE_storm).

SaG morphology and consequently the morphological classes of Duce et al. (2016) can provide further explanations for the mode of wave energy dissipation (Table 1). Where grooves are shorter, they play a critical role in creating steep bathymetric gradients that induce wave breaking (Figures 4 and 8). This differs from previous SaG research (Acevedo-Ramirez et al., 2021) that showed wave breaking being induced by the reef crest. Semi-exposed SaGs (represented here by site OE) are typically shorter (mean length of 71.5 m) and shallower (mean depth of 1.38 m) than the most exposed sites (site OS) and can include both EWE and deep and disconnected (DaD) classes (Table 1). The seaward extent of the EWE grooves at semi-exposed forereef sites (OE; Figure 3d) features a steep bathymetric incline that produces the maximum wave energy dissipation by wave breaking rate observed across all present-day models (1,824.7 W/m^2, Figure 6). As such, long spurs can facilitate frictional dissipation and short grooves can induce wave breaking by introducing steep bathymetric inclines within the breaker zone of incident waves.

The peak in wave energy dissipation shoreward of EWE grooves highlights the complex interaction between forereef morphological evolution and wave energy (Figure 3e). The seaward extent of EWE grooves is at a depth of 3.5 m, coincident with the mean model wave height breaker depth for waves of 1.3–4.3 m (Figure 3, Table 2). As wave breaking imposes forces on the structure of the reef (Massel & Gourlay, 2000; Storlazzi et al., 2005) the results presented here suggest that incident waves could be capable of modifying the EWE grooves in this zone, which is consistent with C14 and U-Th ages of SaG formations on the eastern forereef of OTR (Duce et al., 2020), suggesting an erosive origin for this grooves. Imposed climate change effects further elucidate the influence of grooves. Deep and disconnected (DaD) grooves at site OE exist below the typical wave base and have minimal interaction with present day wave energy. Supporting the previous findings that DaD grooves may be relict features, formed at an early stage during the Holocene transgression (Duce et al., 2016).

4.3. The Impact of Contrasting Forereef Environments on Wave Energy Dissipation Over SaG

Forecasted environmental changes decrease mean wave energy dissipation (Figure 6), which is consistent with other approaches (e.g., Quataert et al., 2015; Sheppard et al., 2005). In the simulations presented here, dissipation remains high between RCP 2.6 and RCP 8.5 as reduced dissipation by bed friction is balanced by an increase in dissipation by wave breaking (Figures 5 and 6). The difference between dissipation by bed friction and dissipation by wave breaking is the greatest at both sites for RCP 8.5, where water depth is still sufficient for wave breaking,

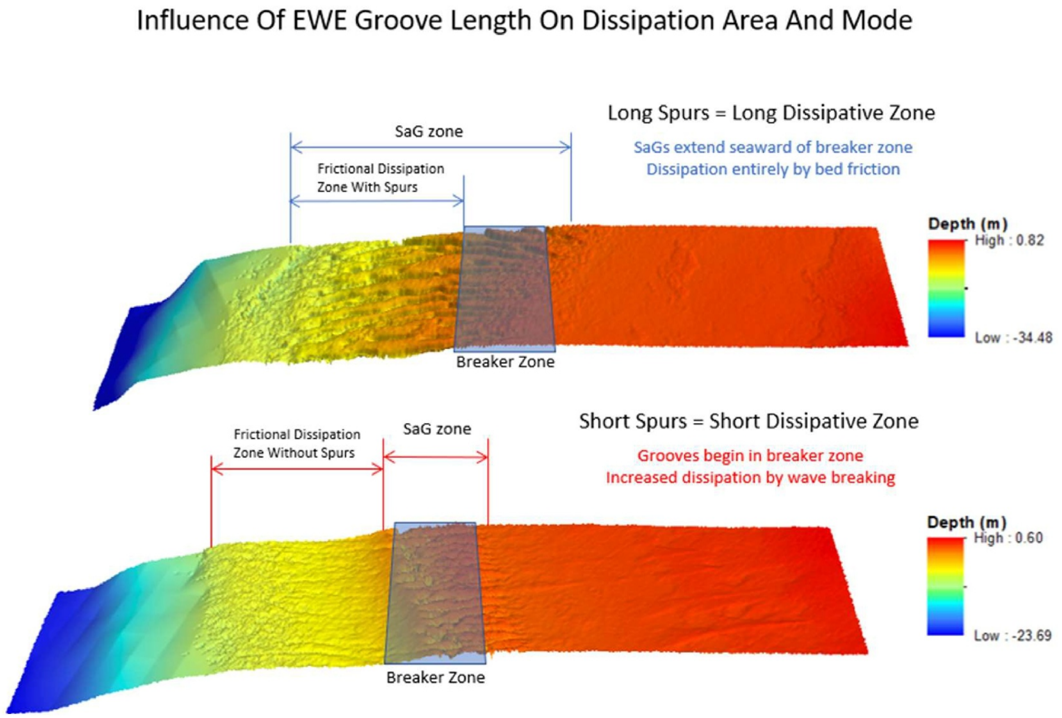

Figure 9. Comparison between exposed and semi-exposed bathymetric profiles (site OS and site OE) demonstrate the influence of the length of the spurs and grooves zone.

yet the degradation of the reef reduces frictional effects (see Figure 8). The reliance on wave breaking dissipation is consistent with observations from high energy reefs of low structural complexity (Harris, Power, et al., 2018). Finally, dissipation is lowest where SLR is greatest (TD scenario) due to waves passing over the reef without breaking (Figure 8). Although the role of SLR is thought to be secondary in contributing to these changes (Harris, Power, et al., 2018), our models suggest that the combined impact of SLR and loss of structural complexity will lead to lowest dissipation rates (Figures 5 and 9) and highest waves at the reef crest(Figures 6 and 9) when climate change parameters (Table 3) were increased between the contrasting forereef environments.

Sea-level rise shifts the region of high energy dissipation toward the reef-crest (Figures 6b, 6c, 6e, and 6f). Bathymetric features that are submerged into the surf zone by rising relative sea level are likely to influence wave breaking and frictional dissipation (Figure 6). This is evident in the shoreward shifting dissipation zones (Figure 6) and as previous literature states (Massel & Gourlay, 2000) is a threat to corals in this zone as wave breaking results in greater hydrodynamic forces on corals. Corals previously protected from wave energy are likely to be species of lower mechanical strength (Storlazzi et al., 2005). Under worse case scenarios (RCP 8.5) by the year 2100, it is likely that corals of the same species may be weaker due to lower carbonate saturation in the water column (Eakin, 1996) or high frequency bleaching events (Hughes et al., 2017). Coral breakage is likely to occur here, and corals that support a steep bathymetric incline with a high frictional coefficient responsible for this peak in wave energy dissipation may have lower structural resilience by 2100 (Eakin, 1996).

High-energy SaG formations have been attributed to wave induced erosion, albeit at vastly different timescales to sedimentary swash-zone features such as rip channels (Duce et al., 2020). It is possible that climate change-driven increase in erosive forces promotes further SaG development on forereefs, which contributes to the dissipation of wave energy.

4.3.1. Increased Wave Transmission at the Reef Crest

Wave transmission at the reef crest increases with increased climate change parameters due to the coupled effects of decreased bed friction and loss of dissipation due to breaking (Figure 6). Compared to mean wave conditions, the impact of storm waves results in an increasingly greater excursion from mean water levels at the reef crest when climate projections are increased (Figure 6). This effect is persistent despite the increased wave energy dissipation at the semi-exposed forereef (site OE) under RCP 8.5 (Figure 3e). The primary control on wave height at the reef crest is SLR, which incorporates eustatic and local sources. Future work should include tidal effects, which would contribute an additional 1.5 m of water level at mean spring high tide at OTR (Harris et al., 2015). The magnitude of wave height increase at the reef crest observed in the TD scenario at an exposed site (OS) of ~4 m is sufficient to entirely flood all backreef environments at OTR, including the low-lying coral island. An increase in wave transmission at the reef crest of this magnitude would have significant impacts on coral reef islands and reef-lined shores (Fellowes et al., 2022; Storlazzi et al., 2015; Talavera et al., 2021). For example, 3.7 m of wave runup combined with sea surface elevation above a reef flat in Roi-Namur, Marshall Islands, was observed in flooding of the inland area of the Island (Cheriton et al., 2016). Research elsewhere demonstrated that wave overtopping on reef islands in the year 2100 will be highly variable across due to variable reef vertical accretion and erosion rates (Beetham & Kench, 2018; Kench et al., 2022), but also due to the vertical accretion of coral reef islands (Kench et al., 2019, 2022; Masselink et al., 2020) which is controlled by sediment availability.

The combined influence of coral reef degradation and SLR amplifies the occurrence of wave transmission beyond the reef crest. Thereby, communities protected by coral reefs are exposed to heightened risks of flooding (Harris, Power, et al., 2018; Quataert et al., 2015; Storlazzi et al., 2018). Notably, a maximum overtopping of approximately 4 m was measured here when the significant wave height reached 5.1 m. An examination of altimeter data reveals that within the 33-year data span, wave heights have not surpassed this threshold (95th percentile wave height = 3.1 m) (Figure S1, supplementary material). Consequently, further investigation is required to determine the frequency of significant overtopping events at the OTR.

5. Conclusion

This study combined numerical modeling and LiDAR-derived bathymetry to demonstrate the importance of forereef spur and groove (SaGs) morphologies in modifying wave energy. Results indicate that high resolution digital elevation models (<1 m) can provide morphometric data to examine wave transformation on forereefs comparable to field studies. We show that groove sinuosity plays a role in wave transformation and should be considered in future research on wave dissipation on SaG. This highlights the need for realistic bathymetry in future studies of forereef wave energy dissipation, as idealized bathymetry used in previous studies, using numerical or physical modeling overlook features such as SaG, which increase wave energy dissipation.

By comparing bathymetry with and without SaG, we demonstrate that SaG morphologies can increase wave energy dissipation by inducing breaking and increasing bed friction. Additionally, SaG morphological classes exhibit distinct dissipation characteristics, with some showcasing higher frictional dissipation and others exhibiting greater breaking dissipation. Notably, spur length emerges as a critical factor in enhancing dissipation by bed friction. Among the SaG morphological classes, EWE grooves have demonstrated the greatest dissipation rates, while DaD grooves contribute less to the dissipation process, particularly when climate change parameters like water level was increased and bed friction factor decreased between each model.

Analyzing the climate change parameters included in each successive model demonstrated that changes in the mode of wave energy dissipation will likely occur. The most notable result was a decrease in dissipation by bed friction from 100% of dissipation under present day conditions to 48% under RCP 8.5. This is matched by a 52% increase in dissipation by wave breaking. Overall, we found a reduction in wave energy dissipation across contrasting forereef environments based on future climate change parameters such as increased water level and decreased bed friction factor. This leads to increased wave transmission at the reef crest, with the maximum transmission occurring where dissipation was lowest. Forereef morphological adjustment to increased dissipation by wave breaking may expose corals to erosion, a process which has been linked to the formation of SaG. The results highlight the critical role of forereef morphology in wave energy dissipation and the need for measures to promote coral growth to facilitate future dissipation.

Data Availability Statement

XBeach version 1.22 (revision 4567) was used in this analysis (Roelvink et al., 2009). Python codes used to interpret bathymetry in XBeach and analyze outputs are available online (Perris, 2024).

Acknowledgments
We acknowledge the Gadigal people of the Eora Nation, the traditional owners of the land and waters where this research was conducted, and pay respects to their elders past, present and emerging. We acknowledge the cultural significance of the Southern GBR, where we conduct fieldwork, to the Tarebilang Bunda, Bailai, Gooreng Gooreng and Gurang Traditional Owners. Lachlan Perris was supported by an RTP scholarship from The University of Sydney and the research was partially funded by ARC Future Fellowship (FT100100215), ARC Discovery Program (DP220101125), and Geoscience Australia funding through the Marine Studies Institute at The University of Sydney. Open access publishing facilitated by The University of Sydney, as part of the Wiley - The University of Sydney agreement via the Council of Australian University Librarians.

References

Acevedo-Ramirez, C. A., Stephenson, W., Wakes, S., & Mariño-Tapia, I. (2021). Wave transformation on a fringing reef system with spur and groove structures. *Journal of Geophysical Research: Oceans*, *126*(9), 1–14. https://doi.org/10.1029/2020JC016910

Amores, A., Marcos, M., Cozannet, G. L., & Hinkel, J. (2022). Coastal flooding and mean sea-level rise allowances in Atoll Island. *Scientific Reports*, *12*(1), 1–12. https://doi.org/10.1038/s41598-022-05329-1

Baldock, T. E., Golshani, A., Callaghan, D. P., Saunders, M. I., & Mumby, P. J. (2014). Impact of sea-level rise and coral mortality on the wave dynamics and wave forces on barrier reefs. *Marine Pollution Bulletin*, *83*(1), 155–164. https://doi.org/10.1016/j.marpolbul.2014.03.058

Baldock, T. E., Shabani, B., Callaghan, D. P., Hu, Z., & Mumby, P. J. (2020). Two-dimensional modelling of wave dynamics and wave forces on fringing coral reefs. *Coastal Engineering*, *155*, 103594. https://doi.org/10.1016/j.coastaleng.2019.103594

Beaman, R. J. (2017). High-resolution depth model for the Great Barrier Reef - 30 M.

Beetham, E., & Kench, P. S. (2018). Predicting wave overtopping thresholds on coral reef-island shorelines with future sea-level rise. *Nature Communications*, *9*(1), 3997. https://doi.org/10.1038/s41467-018-06550-1

Buckley, M. L., Lowe, R. J., Hansen, J. E., & Van Dongeren, A. R. (2016). Wave setup over a fringing reef with large bottom roughness. *Journal of Physical Oceanography*, *46*(8), 2317–2333. https://doi.org/10.1175/JPO-D-15-0148.1

Buddemeier, R. W., & Smith, S. V. (1988). Coral reef growth in an era of rapidly rising sea level: Predictions and suggestions for long-term research. *Coral Reefs*, *7*(1), 51–56. https://doi.org/10.1007/BF00301982

Castillo, K. D., Ries, J. B., Weiss, J. M., & Lima, F. P. (2012). Decline of forereef corals in response to recent warming linked to history of thermal exposure. *Nature Climate Change*, *2*(10), 756–760. https://doi.org/10.1038/nclimate1577

Cheriton, O. M., Storlazzi, C. D., Rosenberger, K. J., McCreary, J. P., & Firing, E. (2016). Observations of wave transformation over a fringing coral reef and the importance of low-frequency waves and offshore water levels to runup, overwash, and coastal flooding. *Journal of Geophysical Research: Oceans*, *121*(9), 6762–6778. https://doi.org/10.1002/2016JC012132

da Silva, R. F., Renan, F., Storlazzi, C. D., Rogers, J. S., Reyns, J., & McCall, R. (2020). Modelling three-dimensional flow over spur-and-groove morphology. *Coral Reefs*, *39*(6), 1841–1858. https://doi.org/10.1007/s00338-020-02011-8

De'Ath, G., Fabricius, K. E., Sweatman, H., & Puotinen, M. (2012). The 27-year decline of coral cover on the great barrier reef and its causes. *Proceedings of the National Academy of Sciences of the United States of America*, *109*(44), 17995–17999. https://doi.org/10.1073/pnas.1208909109

Dechnik, B., Webster, J. M., Davies, P. J., Braga, J., & Reimer, P. J. (2015). Holocene 'turn-on' and evolution of the southern Great Barrier Reef: Revisiting reef cores from the Capricorn Bunker Group. *Marine Geology*, *363*, 174–190. https://doi.org/10.1016/j.margeo.2015.02.014

Duce, S. (2017). *The form, function and evolution of coral reef spurs and grooves*. University of Sydney.

Duce, S., Dechnik, B., Webster, J. M., Hua, Q., Sadler, J., Webb, G. E., et al. (2020). Mechanisms of spur and groove development and implications for reef platform evolution. *Quaternary Science Reviews*, *231*, 106155. https://doi.org/10.1016/j.quascirev.2019.106155

Duce, S., Vila-Concejo, A., Hamylton, S., Bruce, E., & Webster, J. M. (2014). Spur and groove distribution, morphology and relationship to relative wave exposure, southern Great Barrier Reef, Australia. *Journal of Coastal Research*, *70*, 115–120. https://doi.org/10.2112/si70-020.1

Duce, S., Vila-Concejo, A., Hamylton, S. M., Webster, J. M., Bruce, E., & Beaman, R. J. (2016). A morphometric assessment and classification of coral reef spur and groove morphology. *Geomorphology*, *265*, 68–83. https://doi.org/10.1016/j.geomorph.2016.04.018

Duce, S., Vila-Concejo, A., Mccarroll, R. J., Yiu, B., Perris, L. A., & Webster, J. M. (2022). Field measurements from contrasting reefs show spurs and grooves can dissipate more wave energy than the reef crest. *Earth and Space Science Open Archive ESSOAr*, *413*(August 2021), 108365. https://doi.org/10.1016/j.geomorph.2022.108365

Eakin, C. M. (1996). Where have all the carbonates gone? A model comparison of calcium carbonate budgets before and after the 1982–1983 El Nino at Uva Island in the Eastern Pacific. *Coral Reefs*, *15*(2), 109–119. https://doi.org/10.1007/bf01771900

Fellowes, T. E., Vila-Concejo, A., Gallop, S. L., Harley, M. D., & Short, A. D. (2022). Wave shadow zones as a primary control of storm erosion and recovery on Embayed Beaches. *Geomorphology*, *399*, 108072. https://doi.org/10.1016/j.geomorph.2021.108072

Ferrario, F., Beck, M. W., Storlazzi, C. D., Micheli, F., Shepard, C. C., & Airoldi, L. (2014). The effectiveness of coral reefs for coastal hazard risk reduction and adaptation. *Nature Communications*, *5*(1), 3794. https://doi.org/10.1038/ncomms4794

Harris, D. L., Power, H. E., Kinsela, M. A., Webster, J. M., & Vila-Concejo, A. (2018). Variability of depth-limited waves in coral reef surf zones. *Estuarine, Coastal and Shelf Science*, *211*(December 2016), 36–44. https://doi.org/10.1016/j.ecss.2018.06.010

Harris, D. L., Rovere, A., Casella, E., Power, H., Canavesio, R., Collin, A., et al. (2018). Coral reef structural complexity provides important coastal protection from waves under rising sea levels. *Science Advances*, *4*(2). https://doi.org/10.1126/sciadv.aao4350

Harris, D. L., Vila-Concejo, A., Webster, J. M., & Power, H. E. (2015). Spatial variations in wave transformation and sediment entrainment on a coral reef sand Apron. *Marine Geology*, *363*, 220–229. https://doi.org/10.1016/j.margeo.2015.02.010

Harris, D. L., Webster, J. M., Vila-concejo, A., Duce, S., Leon, J. X., & Hacker, J. (2023). Geomorphology defining multi-scale surface roughness of a coral reef using a high-resolution LiDAR digital elevation model. *Geomorphology*, *439*(September 2022), 108852. https://doi.org/10.1016/j.geomorph.2023.108852

Hughes, K., Baird, C., Dietzel, E., Heron, H., Hoogenboom, L., McWilliam, P., et al. (2018). Global warming transforms coral reef assemblages. *Nature*, *556*(7702), 492–496. https://doi.org/10.1038/s41586-018-0041-2

Hughes, T. P., Kerry, J. T., Álvarez-Noriega, M., Álvarez-Romero, J. G., Anderson, K. D., Baird, A. H., et al. (2017). Global warming and recurrent mass bleaching of corals. *Nature*, *543*(7645), 373–377. https://doi.org/10.1038/nature21707

Hughes, T. P., Kerry, J. T., Baird, A. H., Connolly, S. R., Dietzel, A., Mark Eakin, C., et al. (2018). Global warming transforms coral reef assemblages. *Nature*, *556*(7702), 492–496. https://doi.org/10.1038/s41586-018-0041-2

Jell, J. S., & Webb, G. E. (2012). Geology of Heron island and adjacent reefs, Great Barrier Reef, Australia. *Episodes*, *35*(1), 110–119. https://doi.org/10.18814/epiiugs/2012/v35i1/010

Kench, P. S., Beetham, E. P., Turner, T., Morgan, K. M., Owen, S. D., & McLean, R. F. (2022). Sustained coral reef growth in the critical wave dissipation zone of a Maldivian Atoll. *Communications Earth & Environment*, *3*(1), 1–12. https://doi.org/10.1038/s43247-021-00338-w

Kench, P. S., Ford, M. R., & Owen, S. D. (2019). Patterns of island change and persistence offer alternate adaptation pathways for atoll nations. *Nature Communications*, *9*(1), 605. https://doi.org/10.1038/s41467-018-02954-1

Knutson, T. R., Sirutis, J. J., Zhao, M., Tuleya, R. E., Bender, M., Vecchi, G. A., et al. (2015). Global projections of intense tropical cyclone activity for the late twenty-first century from dynamical downscaling of CMIP5/RCP4.5 scenarios. *Journal of Climate*, *28*(18), 7203–7224. https://doi.org/10.1175/JCLI-D-15-0129.1

Lashley, C. H., Dano, R., van Dongeren, A., Buckley, M. L., & Lowe, R. J. (2018). Nonhydrostatic and surfbeat model predictions of extreme wave run-up in fringing reef environments. *Coastal Engineering*, *137*(October 2017), 11–27. https://doi.org/10.1016/j.coastaleng.2018.03.007

Lowe, R. J., Falter, J. L., Bandet, M. D., Pawlak, G., Atkinson, M. J., Monismith, S. G., & Koseff, J. R. (2005). Spectral wave dissipation over a barrier reef. *Journal of Geophysical Research*, *110*(C4), 4001. https://doi.org/10.1029/2004JC002711

Madin, J. S., & Connolly, S. R. (2006). Ecological consequences of major hydrodynamic disturbances on coral reefs. *Nature Letters*, *444*(7118), 477–480. https://doi.org/10.1038/nature05328

Massel, S. R., & Gourlay, M. R. (2000). On the modelling of wave breaking and set-up on coral reefs. *Coastal Engineering*, *39*(1), 1–27. https://doi.org/10.1016/S0378-3839(99)00052-6

Masselink, G., Beetham, E., & Paul, K. (2020). Coral reef islands can accrete vertically in response to sea level rise. *Science Advances*, *6*(June), 3656–3666. https://doi.org/10.1126/sciadv.aay3656

Meucci, A., Young, I. R., Hemer, M., Kirezci, E., & Ranasinghe, R. (2020). Projected 21st century changes in extreme wind-wave events. *Science Advances*, *6*(24), 7295–7305. https://doi.org/10.1126/sciadv.aaz7295

Monismith, S. G., Herdman, L. M. M., Ahmerkamp, S., & Hench, J. L. (2013). Wave transformation and wave-driven Flow across a steep coral reef. *Journal of Physical Oceanography*, *43*(7), 1356–1379. https://doi.org/10.1175/JPO-D-12-0164.1

Monismith, S. G., Rogers, J. S., Koweek, D., & Dunbar, R. B. (2015). Frictional wave dissipation on a remarkably rough reef. *Geophysical Research Letters*, *42*(10), 4063–4071. https://doi.org/10.1002/2015GL063804

Montaggioni, L. F. (2005). History of Indo-Pacific coral reef systems since the last glaciation: Development patterns and controlling factors. *Earth-Science Reviews*, *71*(1–2), 1–75. https://doi.org/10.1016/j.earscirev.2005.01.002

Munk, W. H., & Sargent, M. C. (1948). Adjustment of Bikini Atoll to ocean waves. *Transactions - American Geophysical Union*, *29*(6), 855. https://doi.org/10.1029/TR029i006p00855

Osorio-Cano, J. D., Alcérreca-Huerta, J. C., Osorio, A. F., & Oumeraci, H. (2018). CFD modelling of wave damping over a fringing reef in the Colombian Caribbean. *Coral Reefs*, *37*(4), 1093–1108. https://doi.org/10.1007/s00338-018-1736-4

Pepper, A., & Puotinen, M. L. (2009). Gremo: A GIS-based generic model for estimating relative wave exposure. In *18th World IMACS Congress and MODSIM 2009 - International Congress on Modelling and Simulation: Interfacing Modelling and Simulation with Mathematical and Computational Sciences, Proceedings 1964–70*.

Péquignet, A. C., Becker, J. M., & Merrifield, M. A. (2014). Energy transfer between wind waves and low-frequency oscillations on a fringing reef, Ipan, Guam. *Journal of Geophysical Research: Oceans*, *119*(10), 6709–6724. https://doi.org/10.1002/2014JC010179

Péquignet, A. C., Becker, J. M., Merrifield, M. A., & Boc, S. J. (2011). The dissipation of wind wave energy across a fringing reef at Ipan, Guam. *Coral Reefs*, *30*(SUPPL. 1), 71–82. https://doi.org/10.1007/s00338-011-0719-5

Perris, L. (2024). Lachie-Perris/XBeach_coral: v1.0 (XBeach) [Software]. *Zenodo*. https://doi.org/10.5281/zenodo.10851163

Perry, C. T., Alvarez-Filip, L., Graham, N. A. J., Mumby, P. J., Wilson, S. K., Kench, P. S., et al. (2018). Loss of coral reef growth capacity to track future increases in sea level. *Nature*, *558*(7710), 396–400. https://doi.org/10.1038/s41586-018-0194-z

Quataert, E., Storlazzi, C. D., van Dongeren, A., & McCall, R. (2020). The importance of explicitly modelling sea-swell waves for runup on reef-lined coasts. *Coastal Engineering*, *160*(April), 103704. https://doi.org/10.1016/j.coastaleng.2020.103704

Quataert, E., Storlazzi, C. D., Van Rooijen, A., Cheriton, O., & Van Dongeren, A. (2015). The influence of coral reefs and climate change on wave-driven flooding of tropical coastlines. *Geophysical Research Letters*, *42*(15), 6407–6415. https://doi.org/10.1002/2015GL064861

Reguero, B. G., Losada, I. J., & Méndez, F. J. (2019). A recent increase in global wave power as a consequence of oceanic warming. *Nature Communications*, *10*(1), 1–14. https://doi.org/10.1038/s41467-018-08066-0

Roelfsema, C., Kovacs, E. M., Vercelloni, J., Markey, K., Rodriguez-Ramirez, A., Lopez-Marcano, S., et al. (2021). Fine-scale time series surveys reveal new insights into spatio-temporal trends in coral cover (2002–2018), of a coral reef on the southern Great Barrier Reef. *Coral Reefs*, *40*(4), 1055–1067. https://doi.org/10.1007/s00338-021-02104-y

Roelvink, D., Reniers, A., van Dongeren, A., van Thiel de Vries, J., McCall, R., & Lescinski, J. (2009). Modelling storm impacts on beaches, dunes and barrier islands. *Coastal Engineering*, *56*(11–12), 1133–1152. https://doi.org/10.1016/j.coastaleng.2009.08.006

Rogers, J. S., Monismith, S. G., Feddersen, F., & Storlazzi, C. D. (2013). Hydrodynamics of spur and groove formations on a coral reef. *Journal of Geophysical Research: Oceans*, *118*(6), 3059–3073. https://doi.org/10.1002/jgrc.20225

Rogers, J. S., Monismith, S. G., Fringer, O. B., Koweek, D. A., & Dunbar, R. B. (2017). A coupled wave-hydrodynamic model of an Atoll with high friction: Mechanisms for Flow, connectivity, and ecological implications. *Ocean Modelling*, *110*, 66–82. https://doi.org/10.1016/j.ocemod.2016.12.012

Rogers, J. S., Monismith, S. G., Koweek, D. A., & Dunbar, R. B. (2016). Wave dynamics of a Pacific Atoll with high frictional effects. *Journal of Geophysical Research: Oceans*, *121*(1), 350–367. https://doi.org/10.1002/2015JC011170

Sanborn, K. L., Webster, J. M., Webb, G. E., Carlos Braga, J., Humblet, M., Nothdurft, L., et al. (2020). A new model of Holocene reef initiation and growth in response to Sea-Level rise on the southern Great Barrier Reef. *Sedimentary Geology*, *397*, 105556. https://doi.org/10.1016/j.sedgeo.2019.105556

Saunders, M. I., Simon, A., Roelfsema, C. M., Leon, J. X., Woodroffe, C. D., Phinn, S. R., & Mumby, P. J. (2016). Tectonic subsidence provides insight into possible coral reef futures under rapid sea-level rise. *Coral Reefs*, *35*(1), 155–167. https://doi.org/10.1007/s00338-015-1365-0

Sheppard, C. (1981). The groove and spur structures of Chagos Atolls and their coral zonation. *Estuarine, Coastal and Shelf Science*, *12*(5), 549–560. https://doi.org/10.1016/S0302-3524(81)80081-3

Sheppard, C., Dixon, D. J., Gourlay, M., Sheppard, A., & Payet, R. (2005). Coral mortality increases wave energy reaching shores protected by reef flats: Examples from the Seychelles. *Estuarine, Coastal and Shelf Science*, *64*(2–3), 223–234. https://doi.org/10.1016/j.ecss.2005.02.016

Shinn, E. (1963). Spur and groove formation on the Florida reef tract. *SEPM Journal of Sedimentary Research*, *33*(2), 291–303. https://doi.org/10.1306/74d70e34-2b21-11d7-8648000102c1865d

Shukla, P. R., Skea, J., Slade, R., van Diemen, R., Haughey, E., Malley, J., et al. (2019). IPCC, 2019: Technical summary.

Smith, C., Vila-Concejo, A., & Salles, T. (2023). Offshore wave climate of the Great Barrier Reef. *Coral Reefs*, *42*(3), 661–676. https://doi.org/10.1007/s00338-023-02377-5

Smith, C., Vila-Concejo, A., & Salles, T. B. (2020). RADWave: Python code for ocean surface wave analysis by satellite radar altimeter. *Journal of Open Source Software*, *1*(5), 46. https://doi.org/10.21105/joss.02083

Smyth, C., & Hay, A. A. (2002). Wave friction factors in nearshore sands. *Journal of Physical Oceanography*, *32*(12), 3490–3498. https://doi.org/10.1175/1520-0485(2002)032<3490:WFFINS>2.0.CO;2

Sous, D., Maticka, S., Meulé, S., & Bouchette, F. (2022). Bottom drag coefficient on a shallow barrier reef. *Geophysical Research Letters*, *49*(6), 1–12. https://doi.org/10.1029/2021gl097628

Storlazzi, C. D., Brown, E. K., Field, M. E., Rodgers, K., & Jokiel, P. L. (2005). A model for wave control on coral breakage and species distribution in the Hawaiian Islands. *Coral Reefs*, *24*(1), 43–55. https://doi.org/10.1007/s00338-004-0430-x

Storlazzi, C. D., Elias, E. P. L., & Paul, B. (2015). Many Atolls may be uninhabitable within decades due to climate change. *Scientific Reports*, *5*(1), 1–9. https://doi.org/10.1038/srep14546

Storlazzi, C. D., Gingerich, S. B., van Dongeren, A., Cheriton, O. M., Swarzenski, P. W., Quataert, E., et al. (2018). Most Atolls will be uninhabitable by the mid-21st century because of sea-level rise exacerbating wave-driven flooding. *Science Advances*, *4*(4), 1–10. https://doi.org/10.1126/sciadv.aap9741

Talavera, L., Vila-Concejo, A., Webster, J. M., Smith, C., Duce, S., Fellowes, T. E., et al. (2021). Morphodynamic controls for growth and evolution of a Rubble Coral Island. *Remote Sensing*, *13*(8), 1–23. https://doi.org/10.3390/rs13081582

Yao, Y., Liu, Y., Chen, L., Deng, Z., & Jiang, C. (2020). Study on the wave-driven current around the surf zone over fringing reefs. *Ocean Engineering*, *198*, 106968. https://doi.org/10.1016/j.oceaneng.2020.106968

Young, I. R. (1992). The determination of spectral parameters from significant wave height and peak period. *Ocean Engineering*, *19*(5), 497–508. https://doi.org/10.1016/0029-8018(92)90008-R